Nano Research
2019, 12(5): 1173–1179

ISSN 1998-0124 CN 11-5974/O4
https://doi.org/10.1007/s12274-019-2374-z

Research Article

Highly active zigzag-like Pt-Zn alloy nanowires with high-index facets for alcohol electrooxidation

Yanchao Xu[1], Xiaoqiang Cui[1] (✉), Shuting Wei[1], Qinghua Zhang[2], Lin Gu[2], Fanqi Meng[2], Jinchang Fan[1], and Weitao Zheng[1] (✉)

[1] *State Key Laboratory of Automotive Simulation and Control, School of Materials Science and Engineering, Key Laboratory of Automobile Materials of MOE and Jilin University, Changchun 130012, China*

[2] *Laboratory of Advanced Materials and Electron Microscopy, Beijing National Laboratory for Condensed Matter Physics, Institute of Physics, Chinese Academy of Sciences, Beijing 100190, China*

Received: 8 January 2019 / **Revised:** 4 March 2019 / **Accepted:** 6 March 2019

ABSTRACT

The development of highly efficient Pt-based alloy nanocatalysts is important but remains challenging for fuel cells commercialization. Here, a new class of zigzag-like platinum-zinc (Pt-Zn) alloy nanowires (NWs) with rough surface and controllable composition is reported. The merits of anisotropic one-dimensional nanostructure, stable high-index facets and coordinatively unsaturated Pt sites endow the composition-optimal $Pt_{94}Zn_6$ NWs with a mass activity of 7.2 and 6.2 times higher than that of commercial Pt black catalysts toward methanol/ethanol oxidation, respectively. Alloying-induced *d*-band electron modulation and lattice strain effects weaken the adsorption strength of poisoning species, which originally enhances the catalytic activity of Pt-Zn NWs. This study provides a new perspective of Pt-Zn electrocatalysts with intrinsic mechanism for enhanced catalytic performance.

KEYWORDS

Pt-Zn nanowires, zigzag-like, high-index facets, *d*-band center, strain effects, alcohol oxidation

1 Introduction

Direct alcohol fuel cells (DAFCs), featuring higher energy conversion efficiency and lower environment pollution compared with conventional combustion engines, is holding great potentials to be a practical candidate for future power supply [1–3]. Enormous efforts have been devoted to develop high-performance alcohol oxidation electrocatalysts for DAFCs [4–8]. However, the promise of commercialization for such technologies is still greatly hindered by the high cost of these devices, because a large amount of noble metals such as platinum (Pt) are still indispensable for overcoming the sluggish reaction kinetics of anodic oxidation [9]. Some carbonaceous intermediates such as CO can also strongly adsorb on the catalytic sites during the electrochemical process, leading to the poisoning and passivation of Pt [10]. Indeed, the development of Pt-based electrocatalysts with less Pt loading for simultaneous high catalytic performance and anti-poisoning ability is critical for fuel cell applications.

Previous reports have proven that the Pt-transition metal alloys (Pt-M, M = Ni, Co, Fe, Zn, etc.) with controllable size, structure and composition represent an attractive direction to promote the catalytic performance [11–18]. Except the lower cost after introducing heteroatoms, the ligand effect-induced electronic structure changes and lattice strain effects can also modulate the band structure and chemisorption properties of Pt and in turn lead to a boost on its catalytic activity [12, 19–22]. In search for the efficient Pt-based alloy electrocatalysts, one-dimensional (1D) nanostructures show multiple merits over the zero-dimensional (0D) nanoparticles for catalytic process, including high surface area, fast carrier mobility and inherent anisotropic structure [19, 23–25]. For example, Guo's group and Huang's group have, respectively, demonstrated the hierarchical Pt-Fe and Pt-Co NWs, which all exhibit unprecedented performance towards the oxygen reduction and alcohol oxidation reactions compared with their 0D counterparts [26, 27]. Engineering the nanocatalysts with high-index facets (HIFs) is another effective approach to improve the catalytic performance because the HIFs have high density of steps, edges and coordinatively unsaturated metal atoms, which usually act as active sites for catalytic reaction [26, 28–31]. For instance, Wang's group displayed the synthesis of tetrahexahedral Pt nanocrystals (NCs) bounded with HIFs, which exhibited higher catalytic activities for formic acid and ethanol electro-oxidation than that of spherical counterpart [32]. However, the instability that originates from high surface energy of HIFs renders it still hard to achieve.

Taking these challenges above on, we report a new class of zigzag-like Pt-Zn alloy NWs as efficient catalysts for alcohol electrooxidation in this work. As evidenced by aberration-corrected scanning transmission electron microscopy (STEM), large density of HIFs with abundant coordinatively unsaturated Pt atomic steps are clearly and frequently observed on the uneven surface of each Pt-Zn NW. Fine tuning of the feeding ratio of Pt/Zn precursors affords the final products with controlled composition. The composition-optimal $Pt_{94}Zn_6$ NWs exhibit significantly enhanced electrochemical activities towards methanol and ethanol oxidation reaction (MOR and EOR), i.e., 511.3 $mA \cdot mg^{-1}$ for MOR and 400.0 $mA \cdot mg^{-1}$ for EOR, which are 7.2 and 6.2 times higher than those of commercial Pt black catalysts, respectively. The X-ray analysis and experiments reveal that the alloying effect-induced band structure engineering and lattice strain

Address correspondence to Xiaoqiang Cui, xqcui@jlu.edu.cn; Weitao Zheng, wtzheng@jlu.edu.cn

modulation of Pt-Zn NWs cooperatively weaken the adsorption of poisoning species, which is radically responsible for the enhancement in mass activity.

2 Experimental

2.1 Chemicals

Platinum(II) acetylacetonate ($Pt(acac)_2$, 97%) and oleylamine (OA, 80%–90%) were purchased from Aladdin reagent. Zinc(II) acetylacetonate ($Zn(acac)_2$, 99.9%), glucose ($C_6H_{12}O_6$, ≥99.5%) and commercial Pt black (≥99.97%) were obtained from Sigma-Aldrich. Cetyltrimethylammonium chloride (CTAC, AR), zinc oxide (ZnO, AR) and platinum dioxide (PtO_2, AR) were obtained from Sinopharm Chemical Regent (Shanghai, China). All reagents were used without any further purification. The deionized water (18.2 MΩ·cm^{-1}) was used all through the experiments.

2.2 Characterization

Transmission electron microscope (TEM), high resolution TEM (HR-TEM) and high-angle annular dark-field scanning TEM (HAADF-STEM) images were obtained by using a JEM-2100F TEM (JEOL Co., Japan) working at 200 kV. X-ray diffraction (XRD) patterns were recorded on a Bragg–Brentano diffractometer (D8-tools, Germany) equipped with a Cu Kα emitting source (λ = 1.5418 Å). X-ray photoelectron spectroscopy (XPS) analysis was carried out on an Escalab-250 instrument (Thermo Fisher Scientific, USA) with a hemisphere detector and a monochromatic Al-Kα (1,486.6 eV) radiation source. Inductively coupled plasma mass spectrometry (ICP-MS) tests were measured on an ELAN 9000/DRC ICP-MS system. High-resolution STEM imaging and elemental mapping spectroscopy (EDS) analysis were taken on a JEOL JEM-ARM200F STEM operated at 200 keV.

X-ray absorption fine spectra (XAFS) data was collected at Beijing Synchrotron Radiation Facility (BSRF, operated at 2.5 GeV with a typical current of 250 mA). The Pt L_3-edge (transmission mode) and Zn K-edge (fluorescence mode) X-ray near-edge spectrums (XANES) were tested at 1W1B station at room temperature with a Si (111) double-crystal monochromator. Pt foil and Zn foil measured in transmission mode were used for energy calibration.

2.3 Preparation of zigzag-like Pt-Zn NWs

In a typical synthesis of zigzag $Pt_{94}Zn_6$ NWs, 10 mg $Pt(acac)_2$, 4 mg $Zn(acac)_2$, 20 mg CTAC and 50 mg glucose were added into 5 mL oleylamine. The mixture was vigorously stirred for 30 min to get a uniform solution, and then transformed into a Teflon-lined autoclave. The vessel was sealed and the reaction temperature increased from 30 to 180 °C within 30 min and maintained at this temperature for another 8 h before it was gradually cooled to room temperature. The as-prepared NWs were collected by centrifugation (12,000 rpm, 15 min) and washed with a cyclohexane/ethanol mixture (v/v = 4:1) for three times. The preparation of zigzag-like $Pt_{86}Zn_{14}$ and $Pt_{77}Zn_{23}$ NWs was achieved by tuning the $Zn(acac)_2$ feeding amount from 7 to 10 mg, respectively while keeping other parameters constant.

2.4 Electrochemical measurements

Electrochemical tests were carried on a CHI760E electrochemical analyzer (Shanghai Chenhua Co., China). Catalysts-modified L-type glassy carbon (GC, diameter: 5 mm, area: 0.196 cm^2) electrode, a platinum foil (1 cm × 1 cm) and a calomel electrode were used as working electrode (WE), counter electrode and reference electrode, respectively. The GC electrode was firstly polished with polishing powder and then thoroughly sonicated in ethanol and deionized water before the modification of catalysts. For the preparation of WE, a 5-μL suspension ink of catalyst was dispersed on the GC electrode. MOR and EOR tests were conducted at room temperature with an aqueous solution of 0.1 M $HClO_4$ + 0.2 M methanol/ethanol as electrolytes. Cyclic voltammetry (CV) curves with scanning rate of 50 mV·s^{-1} were applied to evaluate the catalytic performance of different catalysts. The loading amounts of Pt-based catalysts were kept constant in terms of Pt as 18.0 μg·cm^{-2} based on ICP-MS analysis. For performance comparison, the commercial Pt black catalysts were employed with a loading amounts of 25.5 μg·cm^{-2}.

In CO stripping experiments, 0.5 M H_2SO_4 was firstly bubbling high-pure N_2 to drive out the oxygen in electrolyte. Then the catalysts were saturated with CO by bubbling it in the electrolyte for 10 min at −0.1 V (vs. SCE) and N_2 was bubbling again to get rid of the extra CO from the electrolyte for unless 30 min at the same potential. CO stripping voltammograms were performed by scanning the potential between −0.2 and 1.2 V with a sweep rate of 10 mV·s^{-1} (vs. SCE).

3 Results and discussion

The morphology and crystalline feature of as-prepared Pt-Zn NWs were first characterized by TEM. As shown in Fig. 1(a) and Fig. S1 in the Electronic Supplementary Material (ESM), highly uniform NWs with the length longer than a micrometre and the average diameter of 6.24 ± 0.22 nm were the dominant product. High-magnification TEM and HAADF-STEM images (Figs. 1(b) and 1(c)) revealed that each NW had a highly uneven surface with many periodic bumps on it, exhibiting a zigzag-like nanostructure. Continuous lattice fringes in HR-TEM images (Fig. S2 in the ESM) indicated the single-crystalline nature of these zigzag-like NWs. The interplanar spacing was measured to be of 0.223 nm, corresponding to the (111) planes of typical Pt NCs. Strikingly, high density of coordinatively unsaturated atomic steps were clearly observed on the surface of each NW (Figs. S2(b) and S2(d) in the ESM). The aberration-corrected STEM characterization was conducted to thoroughly investigate the atomic structure of as-prepared Pt-Zn NWs. As shown in Fig. 1(d) and Fig. S3 in the ESM, numerous HIFs such as {331}, {221} or even {110} were clearly identified on the uneven surface of these zigzag-like NWs, which could facilitate the chemical bond cleavage and consequently improve the intrinsic activity towards the catalysis process [30, 31, 33]. The composition ratio of Pt/Zn in obtained NWs was determined to be 94/6 by TEM-EDS analysis (Fig. 1(e)), which was consistent with the ICP results. XRD pattern was carried out to identify the crystalline structure of the zigzag-like $Pt_{96}Zn_6$ NWs (Fig. 1(f)) and the results displayed distinct face-centered cubic (fcc) structure with peak positions shifting to higher angle compared to pure Pt crystal, attributable to the alloying effect by replacing Pt atoms with radius-smaller Zn atoms. No detectable peaks of Pt, Zn or zinc oxide phase were detected in XRD pattern, further indicating the phase purity of as-prepared Pt-Zn alloy NWs. The alloy feature of zigzag-like $Pt_{94}Zn_6$ NWs was also confirmed by STEM-EDS elemental mapping analysis (Fig. 1(g)), where the distribution of Pt and Zn were homogeneous through the selected NW.

The composition of as-synthesized Pt-Zn NWs were also modulated by changing the Pt/Zn feeding ratio. Firstly, pure Pt NWs with smooth surface rather than zigzag-like structure bounded with high-indexed atomic steps were obtained in the absence of $Zn(acac)_2$ (Figs. S4(a) and S4(b) in the ESM), which indicated the addition of Zn precursor was crucial in the synthesis of zigzag-like NWs. By tuning the amount of $Zn(acac)_2$ from 4 to 7 and 10 mg, two other Pt-Zn alloy NWs, $Pt_{86}Zn_{14}$ and $Pt_{77}Zn_{23}$ NWs, were also obtained and their nanostructures were also characterized (Fig. 2, Figs. S5 and S6 in the ESM). Similar to the $Pt_{94}Zn_6$ NWs, representative TEM images in Figs. 2(a)–2(d) revealed that all as-prepared NWs possessed a zigzag-like morphology with almost same diameter and highly rough

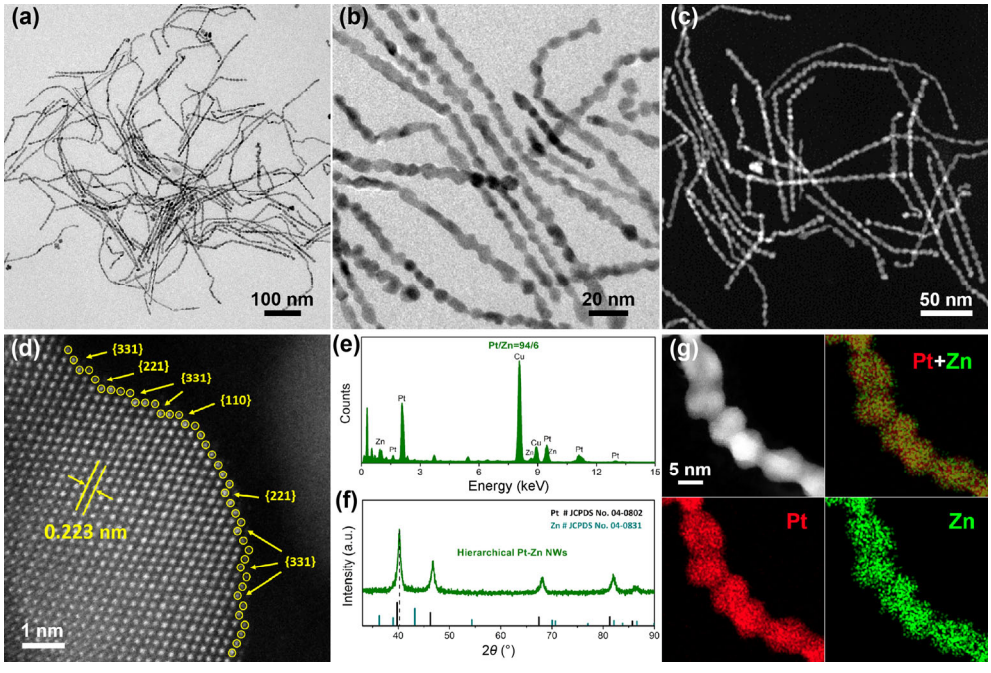

Figure 1 Morphology and structure characterizations of 1D Pt-Zn nanostructures. Representative ((a) and (b)) TEM images, (c) HAADF-STEM image, (d) aberration-corrected atomic-resolution STEM image, (e) TEM-EDS spectrum, (f) XRD pattern and (g) STEM-EDS elemental mapping of as-prepared zigzag Pt-Zn NWs.

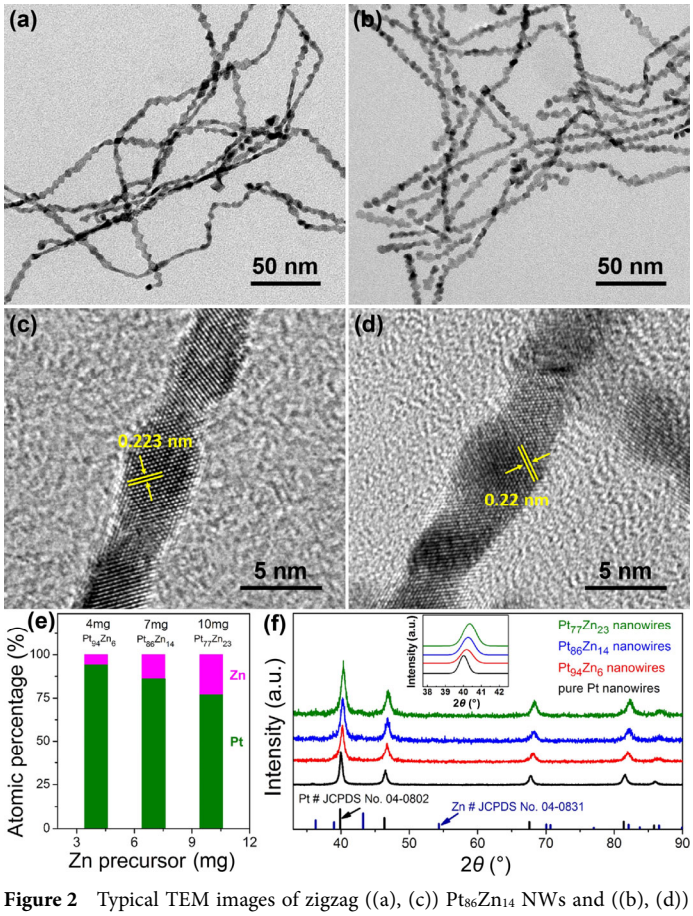

Figure 2 Typical TEM images of zigzag ((a), (c)) $Pt_{86}Zn_{14}$ NWs and ((b), (d)) $Pt_{77}Zn_{23}$ NWs. (e) Composition of Pt–Zn NWs with varying Pt/Zn feeding ratio. (f) Corresponding XRD patterns of the as-prepared Pt-based NWs. Inset shows the amplification of the fitted main peak.

surface. The clear lattice fringes in HR-TEM images (Figs. 2(c) and 2(d)) correspond to a spacing of 0.223 and 0.22 nm, respectively, which agreed with the *d*-spacing of (111) planes of typical fcc Pt. SEM-EDX analysis showed that the Zn atomic percentage in final NWs transforms from 6% to 23% when increasing the Zn amount (Fig. 2(e)). It was also found that XRD peaks of the Pt-based NW were consistently shifted to higher angles as the proportion of Zn increasing (Fig. 2(f)), confirming that the NWs were Pt-Zn alloy NWs. However, further shifting $Zn(acac)_2$ addition to 13 mg produced a lot of inhomogeneous NWs with many spherical impurities (Fig. S4(c) in the ESM).

In order to understand the growth mechanism of this zigzag-like NWs, the reaction time-dependent morphology evolution for $Pt_{77}Zn_{23}$ NWs was carefully investigated by TEM characterization. As shown in Fig. 3(a), ultrathin NWs with a smooth surface and dimeter around 1 nm were clearly obtained at the early synthesis stage (15 min, Fig. 3(a) and Figs. S7(a) and S7(b) in the ESM). Further prolonging the reaction time to 1 and 3 hour, surface of each NW had become more rough (Figs. 3(b) and 3(c)), accompanied by the average diameter increasing to 3 and 4.6 nm, respectively (Fig. S7(c)–S7(f) in the ESM). After the reaction time was increased to 5 h, there was no obvious morphology and diameter change for as-prepared NWs (Fig. 3(d)) compared with our final products. According to the previous reports, the standard reduction potential of Pt is quiet positive than Zn, which means that the Pt precursor is reduced prior to Zn precursor when they coexist [34]. Therefore, we can conclude that the formation mechanism of the Pt-Zn NWs initially involves the synthesis of ultrathin Pt NWs with smooth surface, followed by the reduction of Zn precursor by pure Pt via the underpotential deposition theory [34, 35]. Then, the reduced Zn atoms would diffuse into the Pt lattice to eventually form the alloy phase, during which the different diffusion rate of Pt and Zn may result in the formation of such zigzag-like nanostructures with an uneven surface [27, 36].

Electrocatalytic activities of the resulting zigzag-like Pt-Zn NWs toward anodic oxidation (MOR and EOR) were evaluated by CV and chronoamperometric (CA) techniques with commercial Pt black as benchmark (Fig. S8 in the ESM). The electrochemical active surface areas (ECSAs) from CV curves (Fig. S9 in the ESM) were calculated to be 17.5, 19.1, 18.6, and 12.3 $m^2 \cdot g^{-1}$ for $Pt_{94}Zn_6$ NWs, $Pt_{86}Zn_{14}$ NWs, $Pt_{77}Zn_{23}$ NWs, and Pt black, respectively. The larger ECSA of those Pt-Zn systems indicates that the Pt sites would be more easily exposed and accessible for electrochemical reactions than Pt black catalyst [19, 27]. MOR and EOR tests were carried

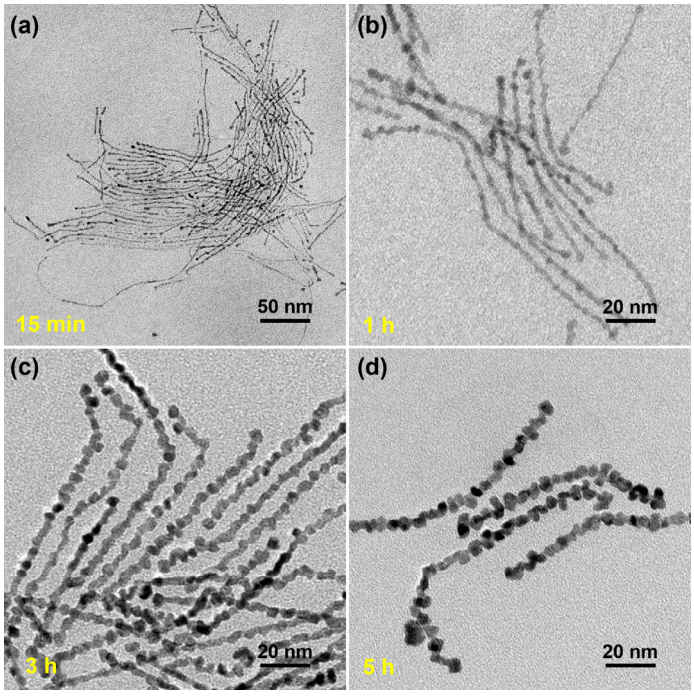

Figure 3 Typical TEM images of zigzag $Pt_{77}Zn_{23}$ NWs intermediates collected from (a) 15 min, (b) 1 h, (c) 3 h and (d) 5 h.

out in 0.1 M $HClO_4$ + 0.2 M methanol/ethanol and their CV curves were shown in Figs. 4(a) and 4(b). The zigzag-like Pt-Zn NWs exhibited enhanced mass and specific activities compared to commercial Pt black (Fig. 4(c) and Fig. S10 in the ESM). For MOR performance, $Pt_{94}Zn_6$ NWs exhibited the highest mass activity (511.3 $mA{\cdot}mg^{-1}_{Pt}$) and specific activity (2.98 $mA{\cdot}cm^{-2}$) among various Pt-based nanomaterials, which were 7.2 and 2.8 times higher than that of Pt black catalysts, respectively. Similarly, superior mass activity (400.0 $mA{\cdot}mg^{-1}_{Pt}$) and specific activity (2.33 $mA{\cdot}cm^{-2}$) of $Pt_{94}Zn_6$ NWs were also determined for EOR tests, which were 6.2 and 2.4 times higher than Pt black, respectively. Long-term stability of Pt-Zn NWs was evaluated with CA curves. As shown in Figs. 4(d) and 4(e), Pt-Zn NWs also possessed better stabilities for both MOR and EOR than Pt black after 3,000 s scanning. Therefore, the better performance in activity and stability makes those zigzag-like Pt-Zn NWs an efficient MOR and EOR catalyst than commercial Pt in acid media.

As we know, the electronic properties and local structures will change when Pt alloys with 3d transition metals, which largely dictates the catalytic performance of a catalyst [37]. X-ray based analysis (XPS, XANES and FT-EXAFS) were hence carried out to investigate the electronic and structural parameters to rationalize the enhanced mass activity of zigzag Pt-Zn NWs (Fig. 5, Figs. S11–S15 and Tabled S1–S3 in the ESM). As shown in Fig. 5(a) and Table S1 in the ESM, an obvious shift of Pt 4f XPS peaks toward high energy level was observed for Pt-Zn alloy NWs compared with the pure Pt NWs, suggesting a mild oxidation state of Pt in Pt-Zn NWs. This positive shift of core-level XPS peak also indicated a down-shift of *d*-band center, which is usually regarded as an efficient descriptor to assess the catalytic activity [38, 39]. Figure 5(b) is the XPS valence band spectra of pure Pt, $Pt_{94}Zn_6$ and $Pt_{77}Zn_{23}$ NWs, where the vertical bars mark out their *d*-band center (3.24, 3.35 and 3.53 eV for pure Pt, $Pt_{94}Zn_6$, and $Pt_{77}Zn_{23}$ NWs, respectively). Pure Pt NWs showed a sharp peak (marked area in Fig. 5(b)) just below the Fermi level while the Pt-Zn NWs showed no immediate peak below the Fermi level, which may be derived from the orbital hybridization of Pt 5d and Zn 3d and suggest the change of *d* electron after introducing Zn [40]. Compared with pure Pt counterpart, the *d*-band center in Pt-Zn NWs was far away from the Fermi level and this down-shift would lead to the decreased adsorption energy between catalyst surface and the adsorbate [41, 42]. CO stripping experiment was conducted to evaluate the adsorption strength of as-prepared Pt-Zn alloy NWs. In Fig. S16 in the ESM, the CO oxidation peak of Pt-Zn was 0.77 and 0.76 V (vs. RHE), which was 80 and 90 mV lower than that of pure Pt NWs (0.85 V vs. RHE), suggesting the decreased adsorption ability on Pt-Zn NWs. XANES analysis at the Pt L_3-edge gave further insight into the electronic and local structure of the catalysts. As shown in Fig. 5(c), the white line intensity of Pt-Zn NWs was more intense than Pt foil, suggesting the mild oxidation state of Pt in Pt-Zn NWs, consistent with the previous XPS analysis. This slight increase in white line peak also indicated that the *d*-electron density of Pt was reduced after alloying with Zn, further denoting the down-shift of *d*-band center [43–45].

We also explored the local structure of Pt atoms by investigating the FT-EXAFS. In Fig. 5(d), the k^3-weighted Pt L_3-edge FT-EXAFS of as-prepared Pt-Zn NWs exhibited a main peak at about 2.6 Å, which corresponded to the Pt–Pt bond. A small shoulder peak located at 1.7 Å was also observed, which represented the Pt–O bond, also indicating the slightly oxidation of Pt in Pt–Zn NWs. An obvious decrease in the main peak intensity of Pt–Zn NW was observed in

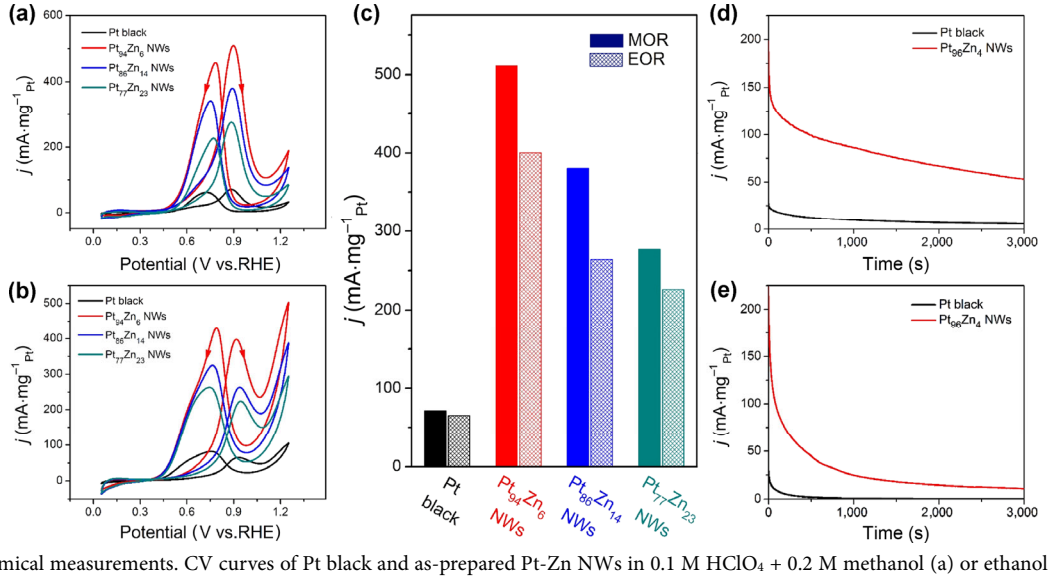

Figure 4 Electrochemical measurements. CV curves of Pt black and as-prepared Pt-Zn NWs in 0.1 M $HClO_4$ + 0.2 M methanol (a) or ethanol (b) at a sweep rate of 50 $mV{\cdot}s^{-1}$. (c) MOR and EOR mass activities of different Pt-based catalysts. CA curves for (d) MOR and (e) EOR recorded at 0.8 V (vs. RHE).

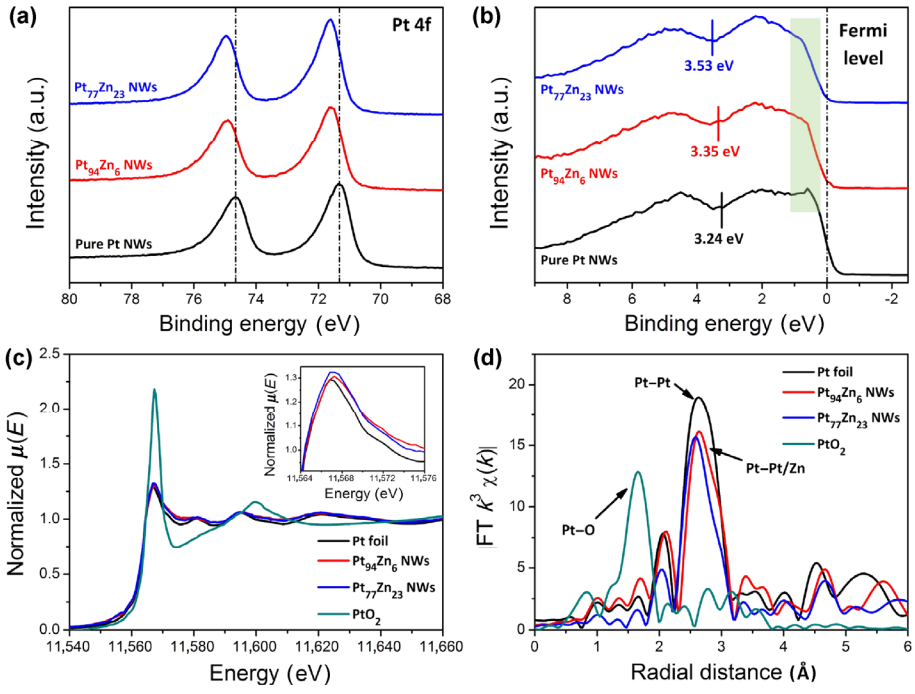

Figure 5 The electronic and local atomic structure analysis of the zigzag Pt-Zn NWs. (a) Pt 4f XPS spectra and (b) XPS valence band spectra of pure Pt, $Pt_{94}Zn_6$ and $Pt_{77}Zn_{23}$ NWs with vertical bars marking out their *d*-band centers; (c) XANES spectra and (d) the k^3-weighted EXAFS spectra for Pt L_3-edge. Inset in (c) shows the enlarged area of white line.

Fig. 5(d) relative to the Pt foil, which indicated the variation in local coordination of Pt species after alloying with Zn atoms, consequently leading to the coordinatively unsaturated Pt sites [46].

FT-EXAFS curves were fitted by the ARTEMS module and the fitting parameters were shown in Table 1. Pt-Zn NWs exhibited a Pt–Pt bond with a coordination number (CN) of 10.1 ± 0.5 and 10.0 ± 0.2, respectively, which was lower than that of 12.0 in Pt foil. This coordinatively unsaturated state of Pt in Pt-Zn NWs was perfectly consistent with the high-indexed feature confirmed by TEM characterization. According to the XRD results and Debye-Scherrer equation, alloying Zn with Pt can induce lattice-strain effect [22, 37]. The $Pt_{94}Zn_6$ and $Pt_{77}Zn_{23}$ NWs possessed a Pt–Pt bond length of 2.76 ± 0.01 and 2.74 ± 0.01 Å, respectively. Although the $Pt_{94}Zn_6$ NWs had little variation in Pt–Pt bond length because of the low Zn content, the shorter bond length in $Pt_{77}Zn_{23}$ NWs than that of Pt foil (2.76 Å) clearly indicated the presence of compressive strain via the alloying effects. Based on previous reports, such lattice strain could improve the catalytic activity by engineering electronic band structure and weakening chemisorption of the intermediate [12, 19, 47]. Therefore, as confirmed by XPS and XAS analysis, the integration of band structure engineering and lattice strain effect contributed the enhanced mass activity of zigzag-like Pt-Zn alloy NWs.

4 Conclusions

In summary, a new class of zigzag-like Pt–Zn alloy NWs with abundant HIFs have been successfully synthesized as efficient electrocatalysts for alcohol oxidation. Composition of these zigzag Pt-Zn NWs is well controlled by tuning the feeding ratio of Pt/Zn precursor. Compared with commercial Pt black catalyst, the composition-optimal $Pt_{94}Zn_6$ NWs shows a 7.2 and 6.2 times higher in mass activity for MOR and EOR, respectively. Combination of XPS and XAS analysis reveals that the alloying effect-induced band structure engineering and lattice strain modulation of Pt-Zn NWs weaken the adsorption strength of poisoning species and in turn are responsible for the enhancement in specific activity. This work not only develops a promising catalyst for the alcohol oxidation but also provides the intrinsic explanation for the enhanced catalytic performance.

Acknowledgements

This work was supported by the National Key Research and Development Program of China (No. 2016YFA0200400), the National Natural Science Foundation of China (Nos. 51571100, 51602305, 51522212, 51421002, and 51672307), Program for JLU Science and Technology Innovative Research Team (JLUSTIRT, 2017TD-09), the Fundamental Research Funds for the Central Universities and the Graduate Innovation Fund of Jilin University.

Electronic Supplementary Material: Supplementary material (additional TEM, HR-TEM, STEM images and XPS analysis of as-prepared Pt–Zn nanowires, detailed structural parameters and FT-EXAFS fitting curves of Pt L_3-edge and Zn K-edge, CV curves, specific activity and CO stripping test of three different Pd-based catalysts) is available in the online version of this article at https://doi.org/10.1007/s12274-019-2374-z.

Table 1 Pt L_3-edge FT-EXAFS fitting results for different Pt-based samples

Sample	Path	CN	*R* (Å)	σ^2 (10^{-3}Å^2)	ΔE_0 (eV)	*R*-factor
Pt foil	Pt–Pt	12.0	2.76 ± 0.00	4.4 ± 0.2	8.63 ± 0.38	0.0020
$Pt_{94}Zn_6$ NWs	Pt–Pt	10.1 ± 0.5	2.76 ± 0.01	5.0 ± 0.3	8.40 ± 0.44	0.0013
$Pt_{77}Zn_{23}$ NWs	Pt–Pt	10.0 ± 0.2	2.74 ± 0.01	6.2 ± 1.0	6.10 ± 0.90	0.0094
PtO_2	Pt–Pt	6.0	3.10 ± 0.03	2.2 ± 0.2	7.40 ± 3.10	0.0011

References

[1] Debe, M. K. Electrocatalyst approaches and challenges for automotive fuel cells. *Nature* **2012**, *486*, 43–51.

[2] Mistry, H.; Varela, A. S.; Kühl, S.; Strasser, P.; Cuenya, B. R. Nanostructured electrocatalysts with tunable activity and selectivity. *Nat. Rev. Mater.* **2016**, *1*, 16009.

[3] Liu, H. L.; Nosheen, F.; Wang, X. Noble metal alloy complex nanostructures: Controllable synthesis and their electrochemical property. *Chem. Soc. Rev.* **2015**, *44*, 3056–3078.

[4] Hunt, S. T.; Milina, M.; Alba-Rubio, A. C.; Hendon, C. H.; Dumesic, J. A.; Román-Leshkov, Y. Self-assembly of noble metal monolayers on transition metal carbide nanoparticle catalysts. *Science* **2016**, *352*, 974–978.

[5] Chen, L.; Lu, L. L.; Zhu, H. L.; Chen, Y. G.; Huang, Y.; Li, Y. D.; Wang, L. Y. Improved ethanol electrooxidation performance by shortening Pd-Ni active site distance in Pd-Ni-P nanocatalysts. *Nat. Commun.* **2017**, *8*, 14136.

[6] Li, H. H.; Fu, Q. Q.; Xu, L.; Ma, S. Y.; Zheng, Y. R.; Liu, X. J.; Yu, S. H. Highly crystalline PtCu nanotubes with three dimensional molecular accessible and restructured surface for efficient catalysis. *Energy Environ. Sci.* **2017**, *10*, 1751–1756.

[7] Dai, S.; Huang, T. H.; Yan, X. X.; Yang, C. Y.; Chen, T. Y.; Wang, J. H.; Pan, X. Q.; Wang, K. W. Promotion of ternary Pt–Sn–Ag catalysts toward ethanol oxidation reaction: Revealing electronic and structural effects of additive metals. *ACS Energy Lett.* **2018**, *3*, 2550–2557.

[8] Song, P. P.; Cui, X. N.; Shao, Q.; Feng, Y. G.; Zhu, X.; Huang, X. Q. Networked Pt–Sn nanowires as efficient catalysts for alcohol electrooxidation. *J. Mater. Chem. A* **2017**, *5*, 24626–24630.

[9] Chung, D. Y.; Yoo, J. M.; Sung, Y. E. Highly durable and active Pt-based nanoscale design for fuel-cell oxygen-reduction electrocatalysts. *Adv. Mater.* **2018**, *30*, 1704123.

[10] Huang, L.; Zhang, X. P.; Wang, Q. Q.; Han, Y. J.; Fang, Y. X.; Dong, S. J. Shape-control of Pt-Ru nanocrystals: Tuning surface structure for enhanced electrocatalytic methanol oxidation. *J. Am. Chem. Soc.* **2018**, *140*, 1142–1147.

[11] Stamenkovic, V. R.; Fowler, B.; Mun, B. S.; Wang, G. F.; Ross, P. N.; Lucas, C. A.; Marković, N. M. Improved oxygen reduction activity on $Pt_3Ni(111)$ via increased surface site availability. *Science* **2007**, *315*, 493–497.

[12] Escudero-Escribano, M.; Malacrida, P.; Hansen, M. H.; Vej-Hansen, U. G.; Velázquez-Palenzuela, A.; Tripkovic, V.; Schiøtz, J.; Rossmeisl, J.; Stephens, I. E. L.; Chorkendorff, I. Tuning the activity of Pt alloy electrocatalysts by means of the lanthanide contraction. *Science* **2016**, *352*, 73–76.

[13] Bu, L. Z.; Zhang, N.; Guo, S. J.; Zhang, X.; Li, J.; Yao, J. L.; Wu, T.; Lu, G.; Ma, J. Y.; Su, D. et al. Biaxially strained PtPb/Pt core/shell nanoplate boosts oxygen reduction catalysis. *Science* **2016**, *354*, 1410–1414.

[14] Jiang, K. Z.; Zhao, D. D.; Guo, S. J.; Zhang, X.; Zhu, X.; Guo, J.; Lu, G.; Huang, X. Q. Efficient oxygen reduction catalysis by subnanometer Pt alloy nanowires. *Sci. Adv.* **2017**, *3*, e1601705.

[15] Mao, J. J.; Chen, W. X.; He, D. S.; Wan, J. W.; Pei, J. J.; Dong, J. C.; Wang, Y.; An, P. F.; Jin, Z.; Xing, W. et al. Design of ultrathin Pt-Mo-Ni nanowire catalysts for ethanol electrooxidation. *Sci. Adv.* **2017**, *3*, e1603068.

[16] Pei, J. J.; Mao, J. J.; Liang, X.; Zhuang, Z. B.; Chen, C.; Peng, Q.; Wang, D. S.; Li, Y. D. Ultrathin Pt–Zn nanowires: High-performance catalysts for electrooxidation of methanol and formic acid. *ACS Sustainable Chem. Eng.* **2018**, *6*, 77–81.

[17] Qi, Z. Y.; Xiao, C. X.; Liu, C.; Goh, T. W.; Zhou, L.; Maligal-Ganesh, R.; Pei, Y. C.; Li, X. L.; Curtiss, L. A.; Huang, W. Y. Sub-4 nm PtZn intermetallic nanoparticles for enhanced mass and specific activities in catalytic electrooxidation reaction. *J. Am. Chem. Soc.* **2017**, *139*, 4762–4768.

[18] Wang, H. J.; Yu, H. J.; Yin, S. L.; Li, Y. H.; Xue, H. R.; Li, X. N.; Xu, Y.; Wang, L. One-step fabrication of bimetallic PtNi mesoporous nanospheres as an efficient catalyst for the oxygen reduction reaction. *Nanoscale* **2018**, *10*, 16087–16093.

[19] Huang, H. W.; Li, K.; Chen, Z.; Luo, L. H.; Gu, Y. Q.; Zhang, D. Y.; Ma, C.; Si, R.; Yang, J. L.; Peng, Z. M. et al. Achieving remarkable activity and durability toward oxygen reduction reaction based on ultrathin Rh-doped Pt nanowires. *J. Am. Chem. Soc.* **2017**, *139*, 8152–8159.

[20] Huang, X. Q.; Zhao, Z. P.; Cao, L.; Chen, Y.; Zhu, E. B.; Lin, Z. Y.; Li, M. F.; Yan, A. M.; Zettl, A.; Wang, Y. M. et al. High-performance transition metal–doped Pt_3Ni octahedra for oxygen reduction reaction. *Science* **2015**, *348*, 1230–1234.

[21] Lu, S. Q.; Zhuang, Z. B. Investigating the influences of the adsorbed species on catalytic activity for hydrogen oxidation reaction in alkaline electrolyte. *J. Am. Chem. Soc.* **2017**, *139*, 5156–5163.

[22] Xiao, W. P.; Cordeiro, M. A. L.; Gong, M. X.; Han, L. L.; Wang, J.; Bian, C.; Zhu, J.; Xin, H. L.; Wang, D. L. Optimizing the ORR activity of Pd based nanocatalysts by tuning their strain and particle size. *J. Mater. Chem. A* **2017**, *5*, 9867–9872.

[23] Li, M. F.; Zhao, Z. P.; Cheng, T.; Fortunelli, A.; Chen, C. Y.; Yu, R.; Zhang, Q. H.; Gu, L.; Merinov, B. V.; Lin, Z. Y. et al. Ultrafine jagged platinum nanowires enable ultrahigh mass activity for the oxygen reduction reaction. *Science* **2016**, *354*, 1414–1419.

[24] Yin, H. J.; Zhao, S. L.; Zhao, K.; Muqsit, A.; Tang, H. J.; Chang, L.; Zhao, H. J.; Gao, Y.; Tang, Z. Y. Ultrathin platinum nanowires grown on single-layered nickel hydroxide with high hydrogen evolution activity. *Nat. Commun.* **2015**, *6*, 6430.

[25] Guo, S. J.; Zhang, S.; Su, D.; Sun, S. H. Seed-mediated synthesis of core/shell FePtM/FePt (M = Pd, Au) nanowires and their electrocatalysis for oxygen reduction reaction. *J. Am. Chem. Soc.* **2013**, *135*, 13879–13884.

[26] Luo, M. C.; Sun, Y. J.; Zhang, X.; Qin, Y. N.; Li, M. Q.; Li, Y. J.; Li, C. J.; Yang, Y.; Wang, L.; Gao, P. et al. Stable high-index faceted Pt skin on zigzag-like PtFe nanowires enhances oxygen reduction catalysis. *Adv. Mater.* **2018**, *30*, 1705515.

[27] Bu, L. Z.; Guo, S. J.; Zhang, X.; Shen, X.; Su, D.; Lu, G.; Zhu, X.; Yao, J. L.; Guo, J.; Huang, X. Q. Surface engineering of hierarchical platinum-cobalt nanowires for efficient electrocatalysis. *Nat. Commun.* **2016**, *7*, 11850.

[28] Zhao, S. L.; Wang, Y.; Dong, J. C.; He, C. T.; Yin, H. J.; An, P. F.; Zhao, K.; Zhang, X. F.; Gao, C.; Zhang, L. J. et al. Ultrathin metal–organic framework nanosheets for electrocatalytic oxygen evolution. *Nat. Energy* **2016**, *1*, 16184.

[29] Zhang, N.; Feng, Y. G.; Zhu, X.; Guo, S. J.; Guo, J.; Huang, X. Q. Superior bifunctional liquid fuel oxidation and oxygen reduction electrocatalysis enabled by PtNiPd core-shell nanowires. *Adv. Mater.* **2017**, *29*, 1603774.

[30] Xu, X. L.; Zhang, X.; Sun, H.; Yang, Y.; Dai, X. P.; Gao, J. S.; Li, X. Y.; Zhang, P. F.; Wang, H. H.; Yu, N. F. et al. Synthesis of Pt-Ni alloy nanocrystals with high-index facets and enhanced electrocatalytic properties. *Angew. Chem.* **2014**, *126*, 12730–12735.

[31] Zhang, N.; Bu, L. Z.; Guo, S. J.; Guo, J.; Huang, X. Q. Screw thread-like platinum-copper nanowires bounded with high-index facets for efficient electrocatalysis. *Nano Lett.* **2016**, *16*, 5037–5043.

[32] Tian, N.; Zhou, Z. Y.; Sun, S. G.; Ding, Y.; Wang, Z. L. Synthesis of tetrahexahedral platinum nanocrystals with high-index facets and high electro-oxidation activity. *Science* **2007**, *316*, 732–735.

[33] Xue, L. F.; Li, Y. C.; Liu, X. F.; Liu, Q. T.; Shang, J. X.; Duan, H. P.; Dai, L. M.; Shui, J. L. Zigzag carbon as efficient and stable oxygen reduction electrocatalyst for proton exchange membrane fuel cells. *Nat. Commun.* **2018**, *9*, 3819.

[34] Chen, Q. L.; Zhang, J. W.; Jia, Y. Y.; Jiang, Z. Y.; Xie, Z. X.; Zheng, L. S. Wet chemical synthesis of intermetallic Pt_3Zn nanocrystals via weak reduction reaction together with UPD process and their excellent electrocatalytic performances. *Nanoscale* **2014**, *6*, 7019–7024.

[35] Zhang, L.; Choi, S. I.; Tao, J.; Peng, H. C.; Xie, S. F.; Zhu, Y. M.; Xie, Z. X.; Xia, Y. N. Pd-Cu bimetallic tripods: A mechanistic understanding of the synthesis and their enhanced electrocatalytic activity for formic acid oxidation. *Adv. Funct. Mater.* **2014**, *24*, 7520–7529.

[36] Day, R. W.; Mankin, M. N.; Gao, R. X.; No, Y. S.; Kim, S. K.; Bell, D. C.; Park, H. G.; Lieber, C. M. Plateau-Rayleigh crystal growth of periodic shells on one-dimensional substrates. *Nat. Nanotechnol.* **2015**, *10*, 345–352.

[37] Li, C. Z.; Yuan, Q.; Ni, B.; He, T.; Zhang, S. M.; Long, Y.; Gu, L.; Wang, X. Dendritic defect-rich palladium-copper-cobalt nanoalloys as robust multifunctional non-platinum electrocatalysts for fuel cells. *Nat. Commun.* **2018**, *9*, 3702.

[38] Stamenkovic, V. R.; Mun, B. S.; Arenz, M.; Mayrhofer, K. J. J.; Lucas, C. A.; Wang, G. F.; Ross, P. N.; Markovic, N. M. Trends in electrocatalysis on extended and nanoscale Pt-bimetallic alloy surfaces. *Nat. Mater.* **2007**, *6*, 241–247.

[39] Wu, Y. S.; Liu, X. J.; Han, D. D.; Song, X. Y.; Shi, L.; Song, Y.; Niu, S. W.; Xie, Y. F.; Cai, J. Y.; Wu, S. Y. et al. Electron density modulation of $NiCo_2S_4$

nanowires by nitrogen incorporation for highly efficient hydrogen evolution catalysis. *Nat. Commun.* **2018**, *9*, 1425.

[40] Abe, H.; Yoshikawa, H.; Umezawa, N.; Xu, Y.; Saravanan, G.; Ramesh, G. V.; Tanabe, T.; Kodiyath, R.; Ueda, S.; Sekido, N. et al. Correlation between the surface electronic structure and CO-oxidation activity of Pt alloys. *Phys. Chem. Chem. Phys.* **2015**, *17*, 4879–4887.

[41] Feng, J. R.; Lv, F.; Zhang, W. Y.; Li, P. H.; Wang, K.; Yang, C.; Wang, B.; Yang, Y.; Zhou, J. H.; Lin, F. et al. Iridium-based multimetallic porous hollow nanocrystals for efficient overall-water-splitting catalysis. *Adv. Mater.* **2017**, *29*, 1703798.

[42] Huang, H. W.; Jia, H. H.; Liu, Z.; Gao, P. F.; Zhao, J. T.; Luo, Z. L.; Yang, J. L.; Zeng, J. Understanding of strain effects in the electrochemical reduction of CO_2: Using Pd nanostructures as an ideal platform. *Angew. Chem.* **2017**, *129*, 3648–3652.

[43] Li, J. R.; Xi, Z.; Pan, Y. T.; Spendelow, J. S.; Duchesne, P. N.; Su, D.; Li, Q.; Yu, C.; Yin, Z. Y.; Shen, B. et al. Fe stabilization by intermetallic $L1_0$-FePt and Pt catalysis enhancement in $L1_0$-FePt/Pt nanoparticles for efficient oxygen reduction reaction in fuel cells. *J. Am. Chem. Soc.* **2018**, *140*, 2926–2932.

[44] Duchesne, P. N.; Chen, G. X.; Zheng, N. F.; Zhang, P. Local structure, electronic behavior, and electrocatalytic reactivity of CO-reduced platinum–iron oxide nanoparticles. *J. Phys. Chem. C* **2013**, *117*, 26324–26333.

[45] Jackson, C.; Smith, G. T.; Inwood, D. W.; Leach, A. S.; Whalley, P. S.; Callisti, M.; Polcar, T.; Russell, A. E.; Levecque, P.; Kramer, D. Electronic metal-support interaction enhanced oxygen reduction activity and stability of boron carbide supported platinum. *Nat. Commun.* **2017**, *8*, 15802.

[46] Cybulskis, V. J.; Bukowski, B. C.; Tseng, H. T.; Gallagher, J. R.; Wu, Z. W.; Wegener, E.; Kropf, A. J.; Ravel, B.; Ribeiro, F. H.; Greeley, J. et al. Zinc promotion of platinum for catalytic light alkane dehydrogenation: Insights into geometric and electronic effects. *ACS Catal.* **2017**, *7*, 4173–4181.

[47] Strasser, P.; Koh, S.; Anniyev, T.; Greeley, J.; More, K.; Yu, C. F.; Liu, Z. C.; Kaya, S.; Nordlund, D.; Ogasawara, H. et al. Lattice-strain control of the activity in dealloyed core-shell fuel cell catalysts. *Nat. Chem.* **2010**, *2*, 454–460.